TECHNISCHE UNIVERSITÄT WIEN
Vienna University of Technology

Diploma Thesis

Magnetron sputtering of Nb–Ag–B thin films for electrical contact applications

carried out for the purpose of obtaining the degree of Dipl.-Ing. submitted at TU Wien, Faculty of Mechanical and Industrial Engineering, by

Stefan Fritze B.Sc.

Mat.Nr.: 0807235

Schulgasse 82/5 1180 Wien, Austria

under the supervision of

Univ.Prof. Dipl.-Ing. Dr.mont. Paul Heinz Mayrhofer
Institute of Materials Science and Technology, E308

Vienna, April 2016

This work was supported by Prof. Ulf Jansson from the Ångström Laboratory, Uppsala University, Sweden

Affidavit

I declare in lieu of oath, that I wrote this thesis and performed the associated research myself, using only literature cited in this volume.

Date

Signature

Acknowledgements

I would like to express my sincerest gratitude to Paul Mayrhofer for welcoming me in his group and for organizing my research semester in Uppsala. Without his help, this Master Thesis would not have been possible.

I am also very grateful to Ulf Jansson for hosting me at Ångström Laboratory and for guiding me through my research in Uppsala.

I want to thank Fedor Klimashin and Paulius Malinovskis for having been great advisors. Thanks to their constant input of ideas, many good results have been achieved.

I want to thank the whole thin film group of the TU Wien for becoming friend over the last year and the thin film group of Uppsala University for giving me a warm welcome to Sweden.

I want to thank Erik Lewin for sharing his clean room experience and helping Svanslos when it did not work properly.

I want to thank Jan Torgersen and Wolfgang Treberspurg for giving a first insight into the field of material science.

I also want to thank my colleagues, my friends and last but not least my family for supporting me.

Table of contents

Abstract

Boron is one of the hardest materials known, and therefore, a promising pathway to achieve high-strength materials is the development of borides, which attracts increasing interest in recent years. While binary, ternary and even quaternary transition metal (TM) nitrides have been studied in detail by experimental and computational materials science, there is only limited information available about TM borides, especially when prepared with physical vapor deposition techniques.

Transition metal diborides (MeB_2) have a wide variety of promising properties such as high hardness, high wear resistance, low friction and high conductivity. An excellent example is the superhard NbB_2 (42 GPa) with low a friction coefficient (0.16) obtained by Nedfors et al.. However, due to a high demand for new materials, binary systems cannot fulfill the newly asked requirements. An interesting approach for improving material properties of sliding electric contacts is the development of ternary borides, where the third element should improve the electric properties while retaining the tribological properties. Silver is one of the best conducting materials, thus it not only retains but even improves the electrical properties. Furthermore, by the addition of Ag also the tribological properties and the toughness are improved. Therefore, we develop materials within the Nb–Ag–B system, where especially $(Nb,Ag)B_2$ phases are of particular interest. However, while there are at least a few reports about NbB_2 thin films, there is only limited and moreover contradictive information available on a crystalline AgB_2 phase.

Based on our results we can conclude that a crystalline AgB_2 phase is not accessible within the wide variation in deposition conditions used during physical vapor deposition. Moreover, newly developed ternary Nb–Ag–B thin films show only crystalline NbB_2 phases with no indication for a solid solution $Nb_{1-x}Ag_xB_2$. For an Ag/(Ag+Nb)-ratio of 0.4, the films exhibit crystalline silver phases next to NbB_2 nanocrystallites. An increase of Ag-content up to Ag/(Ag+Nb)= 0.81 results in a continuous deterioration of hardness from 31 to 2.3 GPa, but also in a significant reduction of compressive residual stresses from 2.3 to 0.13 GPa and friction coefficient from 0.91 to 0.35.

Abstract

Bor ist eines der härtesten bekannten Materialien, und daher ist die Entwicklung von Boriden ein vielversprechender Weg für die Produktion neuer Materialien. Während binäre, ternäre und sogar quasi-ternäre Übergangsmetallnitride bereits experimentell und durch Computersimulation erforscht wurden, gibt es nur wenig Information über Übergangsmetalldiboride, speziell, wenn sie durch physikalische Dampfphasenabscheidung hergestellt wurden.

Übergangsmetalldiboride (MeB_2) haben eine große Zahl von vielversprechenden Eigenschaften wie hohe Härte, hohe Leitfähigkeit, hohe Verschleißfestigkeit, und einen niedrigen Reibkoeffizienten. Ein exzellentes Beispiel dafür ist das von Nedfors hergestellte NbB_2 mit einem Reibkoeffizienten von 0.16 und einem Härtewert von 42 GPa. Aufgrund der immer anspruchsvoller werdenden Anforderungen an neue Materialien reichen oft binäre Systeme nicht mehr aus, um diese Anforderungen zu erfüllen. Ein interessanter Weg für die Verbesserung von elektrischen Kontaktflächen ist die Entwicklung von ternären Boriden, wo das dritte Element nicht nur die elektrischen Eigenschaften beibehält, sondern auch die tribologischen Eigenschaften verbessert. Da Silber ein exzellenter metallischer Leiter ist, verbessert es sowohl die elektrischen als auch die tribologischen Eigenschaften. Daher ist die Untersuchung des Nb–Ag–B-Systems mit einem speziellen Augenmerk auf eine mögliche $(Nb,Ag)B_2$ Phase von großem Interesse. Im Gegensatz zu NbB_2 gibt es zu AgB_2 bisher nur widersprüchliche Informationen.

Aus unseren Ergebnissen können wir schließen, dass eine kristalline AgB_2 Phase trotz der vielfältig eingesetzten Möglichkeiten der physikalischen Dampfphasenabscheidung nicht synthetisiert werden konnte. Des Weiteren wurden ternäre Ng–Ag–B-Dünnschichten entwickelt, welche jedoch nur eine kristalline NbB_2 Phase aufweisen, aber keine Anzeichen für eine Mischkristallbildung $Nb_{1-x}Ag_xB_2$ zeigen. Für ein Verhältnis Ag/(Ag+Nb) von 0.4 setzten sich die Schichten sowohl aus kristallinem Ag als auch aus kristallinem NbB_2 zusammen. Eine Zunahme des Ag-Gehalts bis zu einem Verhältnis Ag/(Ag+Nb) von 0.81 resultiert in einer Härteabnahme von 31 auf 2.3 GPa und einer signifikanten Verringerung des Reibkoeffizienten von 0.91 auf 0.35.

1. Introduction

The first chemical or mechanical contact between a material and its surroundings occurs on its surface. Therefore, the properties and the performance of a bulk material can be improved to an enormous extent modifying the surface e.g. by depositing a thin film on the surface. The film properties can be tailored in a way that the material combines high hardness, high wear resistance, low friction and high electrical conductivity. Consequently, thin films are used in many industrial branches such as machining, microelectronics and semiconductors. Since the 1960`s thin film technology has become a large industry sector. The commercial demand on new materials increases, and often traditional ways of improving them are not sufficient anymore.

For modern society the performance of electrical contacts is crucial since they are used in power grids and other applications. The "Energiewende" taking place in Europe leads to a demand of special electrical contact materials for renewable energy power plants. As they are not providing energy at a constant level, much more switching in the power grids is required. A traditional electrical contact member consists of a cheap and highly electrically conductive bulk metal (e.g. aluminum or copper) which is coated with a noble metal (e.g. silver or gold). The good electrical contact properties result from the coating, giving the contact a high corrosion resistance and low electrical contact resistance. However, for sliding electrical contacts pure noble metals are not suited, as they exhibit a high coefficient of friction and a low wear resistance. Hence, it is of great interest for industry to find new electrical contact materials, particularly for switching and sliding application. One approach is to completely replace silver towards other contact materials. In cooperation with ABB Corporate Research in Västerås, Sweden, the thin film group of Uppsala University has investigated the use of nanocomposites materials, such as nc-TiC/a-C or nc-NbC/a-C, as electrical contact materials in detail [2,3]. Furthermore, Nedfors has investigated NbB_2 which exhibits a low COF in combination with superhardness [1]. All nanocomposite materials showed promising tribological properties and a low contact resistance, though these materials face ageing problems such as oxidation. An alternative solution is to use multiphase materials where Ag is combined with other phases in a nanocomposite material. ABB has therefore initiated a new project together with Uppsala University where multiphase structured thin films containing Ag are investigated as possible new contact materials. The requirements on the additional phase are to

reduce the COF (< 0.3), increase wear resistance while maintaining a low contact resistance over the life time of 30 years. A recent example is the Cr–C–Ag system studied by Folkenant et al. [4].

The focus of this project is to investigate films in the Nb–Ag–B system as potential contact materials and is separated into three parts.

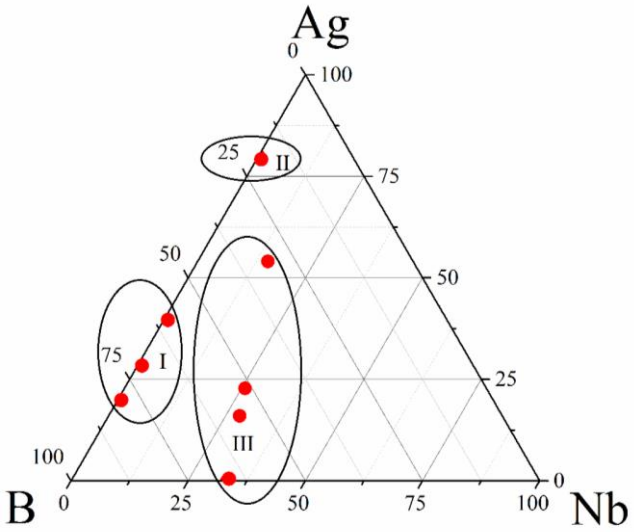

Figure 1: Ternary Nb–Ag–B system

In the first part, we investigated the existence of a superconducting AgB_2 phase which has been reported in literature [5]. An Ag/AgB_2 film could be a superior contact solution. In the second part, we alloyed Ag with 20 at.% B, where the lubricant H_3BO_3 is expected to form during operation, reducing the COF against an Ag counterpart while maintaining the low contact resistance of silver. In the third part, we explored Nb–Ag–B films which should combine the low COF of NbB_2 with the low contact resistance of Ag. Within the Nb–Ag–B system a metastable $Nb_{1-x}Ag_xB_2$ solid solution may be obtained for a low Ag-content. For a high Ag-content the growth of crystalline NbB_2 and Ag is excepted.

2. Transition metal borides

Transition metal borides are compounds consisting of a transition metal (Me) and boron. In literature reports, a variety of TM borides is available in a wide composition range. For transition metal diborides (MeB_2), several different crystalline structures have been reported. In the framework of this thesis, we focus on the synthesis of AlB_2-type structure MeB_2. The AlB_2 structure is the most common structure for MeB_2 containing a transition Me from the groups 4 to 6. Figure 2 represents the AlB_2-type structure (space group P6/mmm) with a simple hexagonal lattice consisting of the hexagonal boron planes separated by the metal layers. The boron atoms are arranged in graphite-like hexagons, while the metal atoms are centered above (and below) these hexagons [6]. The borides combine, similar to carbides, a mixture of covalent, ionic and metallic bonding [7]. The strong covalent bonding results from the B-B bonds as suggested by calculations of the electronic structure of the AlB_2-structured MeB_2 [8]. The transition metal (Me) and boron (B) atoms are predominantly linked by covalent bonds, with a charge transfer predicted by calculations towards the B atoms, leading to an ionic contribution [8]. An increase of valence electrons for the Me atom leads to a decrease of the ionic contribution.

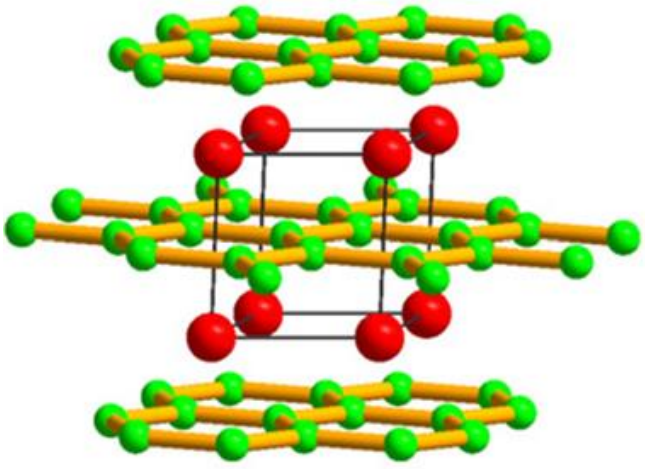

Figure 2: AlB_2-type structure with B (red spheres) and Me (green spheres) [6]

For AlB_2-structured MeB_2, density of state (DOS) calculations and the band structure have been reported [9,10]. The typical DOS has a pseudo gap delinking the non-bonding and antibonding

states from the bonding states. The Fermi level for group 4 Me is in the middle of the pseudo gap, and thus, the bonding states are fully occupied. Therefore, borides formed with group 4 Me are the most stable with a formation enthalpy of around -1 eV/atom [8,9] (Figure 3). DFT calculations of group 5 and 6 transition metals in MeB_2 suggest an improved stability by reducing the number of filled antibonding states.

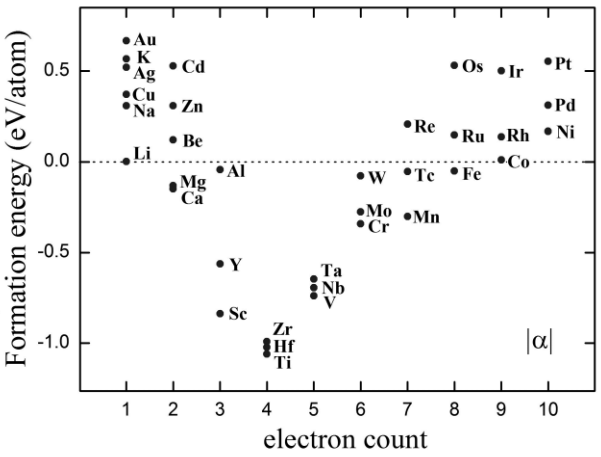

Figure 3: Calculated formation energies for AlB_2 structured borides [9]

Transition metal diborides exhibit excellent properties such as high hardness, high wear resistance, chemical inertness, low friction and high/super conductivity [1,11] and are therefore of interest for various industrial applications. For example NbB_2 exhibits hardness of ~42 GPa [1] and MgB_2 is a superconductor with T_c of 39 K [11]. Such excellent properties can be obtained when synthesizing diborides with AlB_2-type structure. Many diborides exhibit AlB_2-type structure only on a small chemical composition range. Nunes et al. showed that AlB_2-type structure can be obtained for NbB_2 in sub- and overstoichiometric films ($NbB_{1.86}$-$NbB_{2.34}$), and it is therefore an exception [12]. For some elements such as silver, crystallization in the AlB_2-type structure is predicted through theoretical calculations, although there is no experimental confirmation. Furthermore, several papers report that the crystalline AgB_2 phase does not form [13,14].

In 2001, superconductivity in the intermetallic compound MgB_2 (AlB_2-type structure) with a transition temperature of 39 K was reported [11]. The electronic p-states of boron are essential for the superconductivity in AlB_2-type compounds [9]. This finding has triggered a search for further superconducting borides. AgB_2 is of particular interest since noble metals are already used in many electronic applications, and their performance could possibly be improved by noble metal

diborides. Moreover, the ion radii of Ag and Mg are close to each other, suggesting thus the possibility of formation of AgB_2 phase [15]. Boron exhibits superconductivity only under very high pressure (250 GPa), and noble metals such as silver and gold are non-superconducting, which distinguishes them from transition metals. Nevertheless, superconductive behavior in noble metal compounds such as AgB_2, AuB_2 and CuB_2 is predicted through theoretical investigations by different authors. Kwon et al. predicted the transition temperature for AgB_2 to be 59 K and explained such a high value through the stronger electron-phonon coupling constant and the higher density of states on the Fermi surface [14]. Recent calculations predict a significantly lower T_c at 7.4 K caused by spin fluctuation [16].

The existence of AgB_2 is contradictory, however the phase diagram database shows a stable AgB_2 phase at room temperature; see Figure 4. Obrowski claimed in 1961 to obtain an AgB_2 phase with cell parameters: a = 0.300 nm and c = 0.324 nm [5]. Further X-ray investigations in the 60's could not verify his findings [17]. Koutna calculated a formation enthalpy of 0.487 eV/atom for Obrowski´s cell parameters which correlates well with 0.483 eV/atom published by Ying [10]. For compounds with positive formation enthalpy, extreme synthesis conditions such as high temperature and/or high pressure are needed, and therefore, many different techniques such as spark plasma sintering, pulsed laser deposition, physical vapor deposition, and high-energy ball milling were used to access the AgB_2 phase.

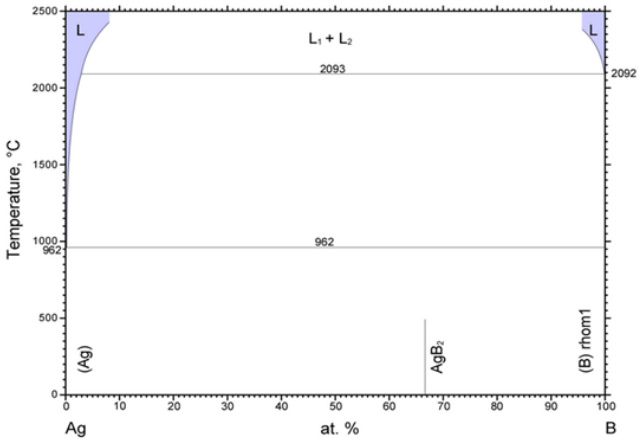

Figure 4: Ag–B phase diagram [5]

Tomita et al. reported on the superconductivity in thin films which were prepared by pulsed laser deposition (PLD) from a target with a nearly stoichiometric AgB_2 composition [15]. The observed

transition temperature of 6.7 K is far below from the predicted 39 K by Kwon et al. [14] and the XRD pattern showed no AgB_2 peaks.

Pelleg et al. prepared Ag–B thin films by magnetron co-sputtering from the two separate targets. The XPS spectrum shows a shift of the B peak towards higher energies, which indicates the existence of Ag–B bonds, while the asymmetry of this peak indicates the existence of the B–O bonds. The observed peak at ~28 degree in the XRD pattern (Figure 5) can be attributed either to AgB_2 or to B_2O_3. Even though the results were promising no superconductive behavior was observed down to 10 K [18].

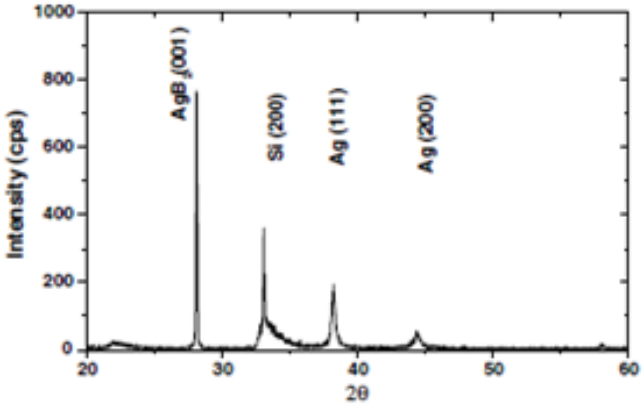

Figure 5: XRD scan with a possible AgB_2 phase [18]

3. Thin film deposition techniques

For the synthesis of thin films different methods, such as physical- and chemical vapor deposition, are used. These two major techniques differ by the means of supplying the necessary vapor for the deposition process. Within the framework of this thesis only the PVD process magnetron sputtering was used.

3.1. Physical Vapor Deposition

Physical vapor deposition (PVD) has been an often used and important technique to modify the surface properties of tools in different applications for over 50 years [19]. The major upside of PVD over other industrially implemented deposition techniques, such as chemical vapor deposition (CVD), is the high number of accessible target materials and the lower substrate temperature, often around 300 °C, which allows to lower the requirements to the substrate materials.

All PVD processes follow three steps:

- phase conversion of the target material from solid into vapor;
- transfer of vapor from source to the substrate;
- condensation of vapor, nucleation, and film growth

Depending on the mechanism of the phase transition from solid phase to vapor, all PVD techniques fall essentially into two big categories: sputtering and evaporation. The phase conversion during sputter deposition is based on the momentum transfer from an ionized working gas to the target material, whereas the evaporation process is based on a thermal energy input. Ion plating can be seen as a combination of sputtering and evaporation.

A simple sputtering system consists of two parallel electrodes (anode and cathode) enclosed in the vacuum chamber (Figure 6). After introducing a working (inert) gas (usually Ar) into the chamber it becomes ionized through collision with the primary electrons. The sputtering process begins by generating low-current high-voltage glow discharge. The ionization process is accompanied by a release of the secondary electrons acting in the plasma as primary electrons, thus triggering the chain reaction by increasing the collision probability. By applying a negative voltage to the target, the positively charged working gas ions accelerate towards and bombard the target surface where

they scatter inelastically. Through the momentum transfer, atoms (or atomic clusters) of the target material are ejected, move subsequently towards the substrate and condense finally on its surface forming a film.

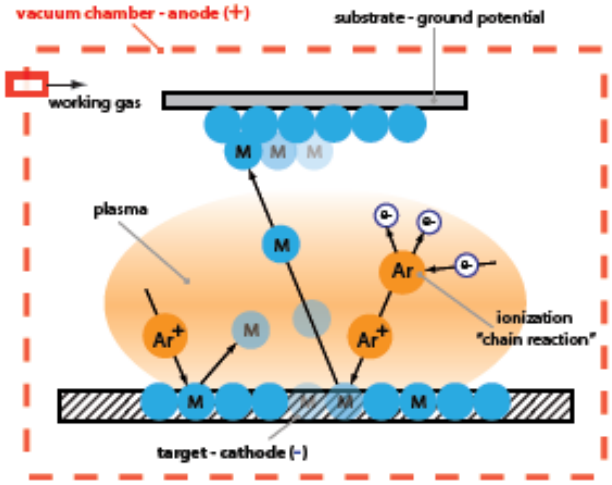

Figure 6: Schematic of basic sputter process [20]

One parameter which is often used to describe the coating efficiency is the sputter yield (Y), defined as the "ejected atoms-incident ions" ratio, i.e. the number of ejected atoms from the target compare with the number of incident working gas ions. Many parameters, such as energy of the incident ions or the binding energy of the target atoms, influence the sputter yield [19].

Sputtering with a direct current (DC) power supply is an easy and cheap coating process. A constant direct current potential in the magnitude of hundreds of volts is introduced between the positively charged chamber walls with substrate and the negatively charged target. DC sputtering is limited to conductive materials, since by sputtering of insulators, charging effects occur. This effect is accompanied by formation of a charged interface on the target surface, which acts as a barrier for arriving ions, thus decreasing the sputter yield or stopping completely the process. This can also result in undesirable arc ignition [21].

4. Thin film growth

Thin film properties are strongly influenced by the deposition conditions and can be modified by varying the chamber pressure, the substrate temperature and the bias voltage. During the formation of a film, nucleation and growth processes take place. The film growth starts with the condensation of vaporized target atoms on the substrate surface. These atoms typically have a kinetic energy of a few electron volts. The ad-atoms diffuse along the substrate surface to energetically optimal positions. Once the ad-atom clusters reach a critical size (> 0.1 nm), nucleation starts and a larger number of atoms arriving at the surface favors a state with reduced total surface energy. The crystallite sizes increase with the incorporation of arriving atoms continuously, which also leads to an increased island density. In the next step, secondary nucleation and coalescence takes place, the latter works however counterproductively, reducing the island density [19].

Film growth can be explained by three basic different modes (Figure 7) [22]. These differ by the binding energy between the arriving atoms and the substrate. The Frank van der Merwe or layer by layer film growth (2D growth mode) occurs if the adding atoms are stronger bonded to the substrate than to each other. Due to the surface energy the formation of a new layer will not start until the entire surface underneath is covered. The single-crystal epitaxial growth of semiconductors is an important example of the 2D mode. The Vollmer-Weber mode is a 3D growth mode and occurs if the atoms are stronger bonded to each other than to the substrate. Many metals (i.e. Ag) exhibit this growth mode on insulating substrates. The Stranski-Kastranov growth is a two-step mode combining the two described concepts [23]. In the first step, a few monolayers grow in the 2D mode switching to the then energetically favorable 3D growth mode in the second step.

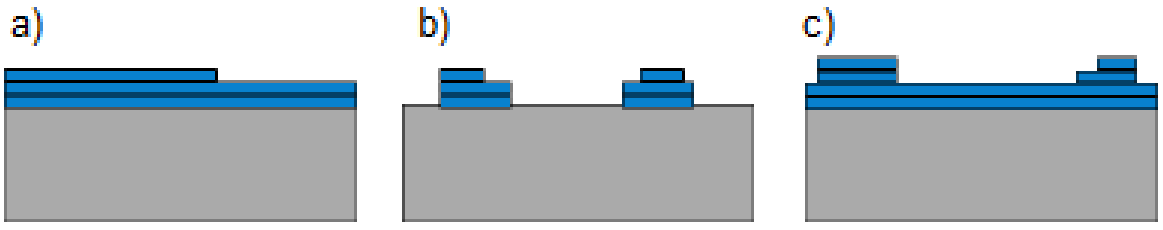

Figure 7: a) Frank von der Merwe; b) Vollmer-Weber c) Stranski-Kastranov [24]

5. Structure zone model

The structure zone model (SZM) was developed to display the influence of different deposition parameters on the film microstructure. Movchan and Demchishin [25] introduced a SZM, consisting of three zones for thick (> 100 µm) polycrystalline films depending on the homologous temperature (T_h). The reduced parameter T_h is defined as the film growth temperature normalized by the melting point of the deposited film material. Thorton [26] enhanced the model by adding two crucial parameters, deposition pressure and the substrate temperature, and introducing the transition zone between zone I and II. Later, Messier [27] explained the ion energy as a further important factor. Modern PVD processes are best described by the SZM described by Anders (Figure 8) [28]. In this model the generalized temperature T* and the normalized energy E* are used as main axis. T* includes the homologous temperature and a temperature shift induced by the potential energy of arriving particles. E* describes heating and displacement effects and replaces the linear pressure axis. The net film thickness t* on the z-axis provides information about the film thickness resulting from ion etching, sputtering and densification.

As described in the previous paragraph, one can distinguish four different zones in the SZM. In zone 1, delimited by low deposition temperatures and low E* values, a low ad-atom mobility leads to a porous and/or amorphous morphology. The transition zone, located between zone 1 and zone 2, exhibits a fine grained and dense microstructure. In zone 2, higher temperatures and energies are leading through an enhanced surface mobility and diffusion of ad-atoms to a dense columnar grained microstructure. Bright surfaces and large grains are observed in zone 3 as a result of recrystallization and bulk diffusion processes caused by higher energies and temperatures than in the previous zone. A further increase of particle energies leads to a decrease of deposition rate as a result of film densification or re-sputtered particles. At very high E* the SZM shows an area with negative film thickness due to a higher number of re-sputtered than arriving atoms. This effect is used for the cleaning of the substrate before the film deposition and is often called plasma etching.

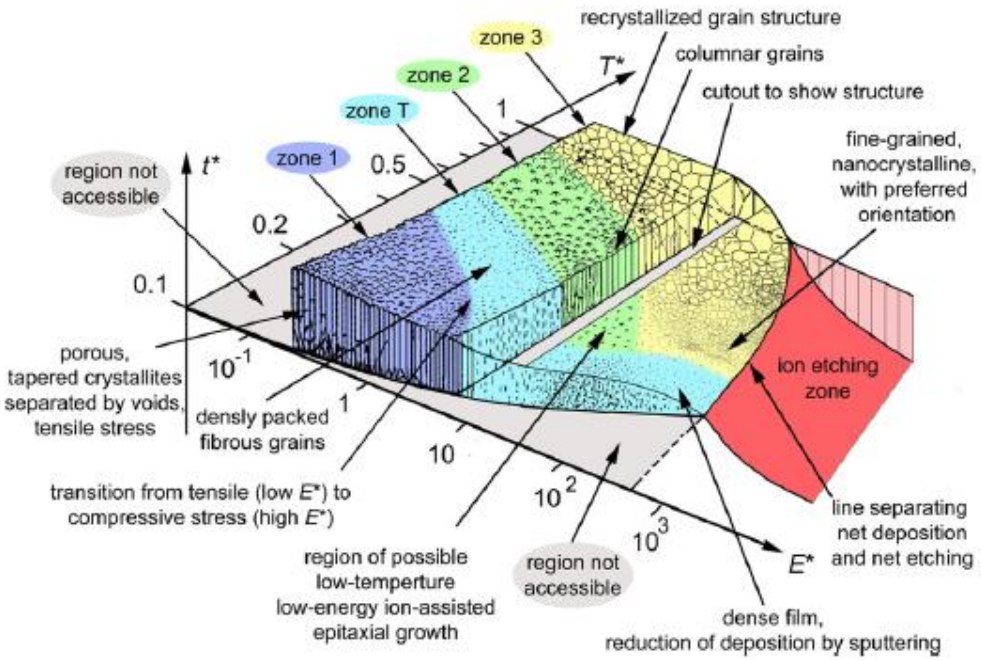

Figure 8: Stucture zone model by Anders [28]

6. Characterization techniques

For a better understanding of the material behavior, many properties, such as microstructure and hardness, have to be investigated in detail. The following chapter will give a brief overview of the characterization methods used within this thesis.

6.1. X-ray photoelectron spectroscopy

XPS is based on the photoelectronic effect and often used for elemental analysis. XPS is mainly used for surface analysis in general and more specific for thin films in microelectronics or hard coatings. This technique has a very high surface sensitivity, thus obtaining the information from the first few monolayers of the sample.

The photoelectronic effect occurs when a material is irradiated by X-rays and electrons (photoelectrons) are ejected out of the material. The energy needed to remove the electrons (E_b) can be calculated with following equation [29]:

$$E_b = h\nu - E_k - \Phi \qquad (1)$$

where $h\nu$ is the energy of the X-ray photons, E_k – the measured kinetic energy of the photoelectrons, Φ – the work function, which is a constant for the detector material. The chemical composition of our films was determined from the depth profile measurements carried out by X-ray photoelectron spectroscopy (Physical Systems Quantum 2000 with monochromatic X-ray Al Kα radiation). The B1s spectra of the film surface and of the wear track were acquired after 30 min of 200 eV Ar^+-ion sputtering in order to remove contaminations which could be on the surface after the tribological test.

6.2. X-ray diffractometry

The crystal structure of a material is a determining factor of its properties such as hardness or electrical and thermal conductivity. The most common way to analyze the crystal structure of materials is X-ray diffraction (XRD). Diffraction occurs when electromagnetic radiation such as X-rays interacts with a periodic structure of atoms. The bonding length in crystals is 0.15 - 0.4 nm, which corresponds to the wavelength of X-rays with energies between 3 and 8 keV. The X-rays

introduce an electromagnetic field which interacts with the electron shells of an atom. This interaction leads to the emission of photons with similar energy to the impinging radiation. The ability to scatter depends on the atomic number and the states of the electrons. The scattered electromagnetic waves can either constructively or destructively (Figure 9) interfere, depending on the present atomic structure. Constructive interference only occurs, when the lattice plane distance d_{hkl} fulfills the Bragg's law:

$$n \cdot \lambda = 2 \cdot d_{hkl} \cdot sin\,\theta \qquad (2)$$

Equation (2) shows Bragg´s law, where λ is a given wavelength (Cu Kα radiation with λ = 1.5406 Å was used in our study), d_{hkl} is the lattice plane distance, θ is Bragg´s angle, and n is the diffraction order [30].

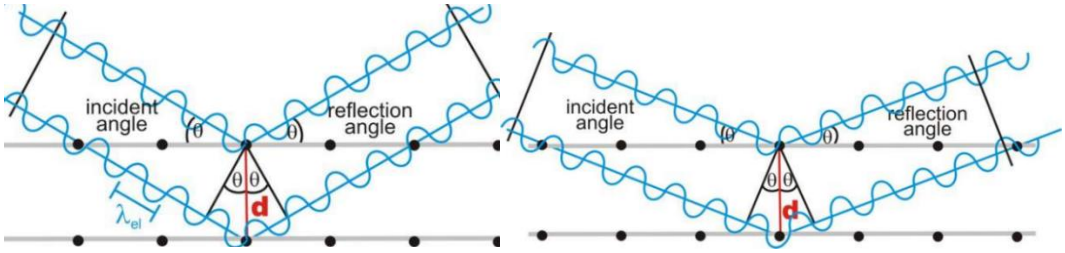

Figure 9: Bragg-diffraction [31]

Two different setups were used in this work to obtain information about crystal structure of the deposited films. In the Bragg-Brentano geometry (Figure 10), the angle of the incoming X-rays (θ) is the same as the angle of the detected outgoing X-rays (θ), and thus, this method is often called „θ-2θ scan". Only the X-ray waves scattering on the crystal planes parallel to the surface and fulfilling the Bragg's law are detected. Thus, besides the phase composition, the information about the preferential grain orientation with respect to the substrate surface can be obtained.

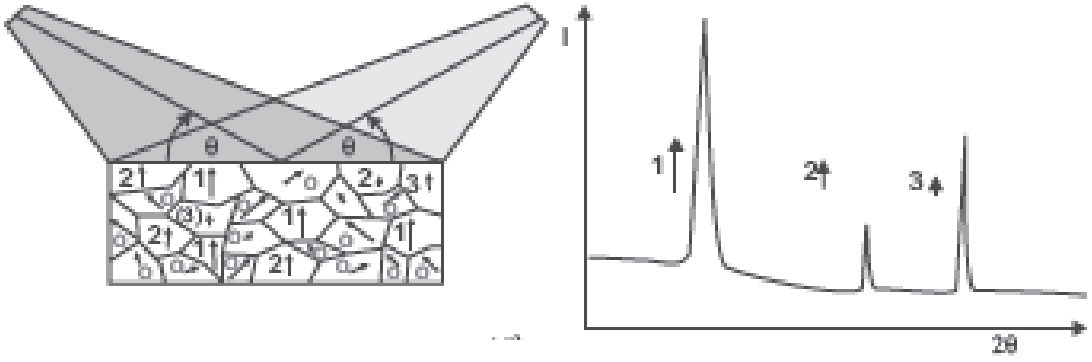

Figure 10: Bragg-Brentano diffraction [30]

The penetration depth of the X-rays into the material can be calculated using the following equation:

$$x_e = \frac{sin(\theta_i)sin(\theta_o)}{\mu(sin(\theta_i)+sin(\theta_o))} \qquad (3)$$

where x_e corresponds to the penetration depth, θ_i is the incoming angle, θ_o is the outgoing angle and μ is the linear absorption coefficient and, thus, a function of the X-ray energy and the material density [32].

In order to simplify the phase analysis, single-crystal or amorphous substrates are used. For the analysis of thin films the grazing incidence X-ray diffraction (GIXRD) setup was developed. The main difference from GIXRD to the Bragg-Brentano setup is the angle of the incoming beam, which is held constant at a small, grazing angle (only a few degrees), and only the detector moves with an angle 2θ. As the scattering vector is not constant anymore, all lattice planes (and not only the parallel ones) contribute to the X-ray diffraction pattern. The incoming X-rays travel a much longer path within the film, and so, the probe volume can be significantly increased [33,34].

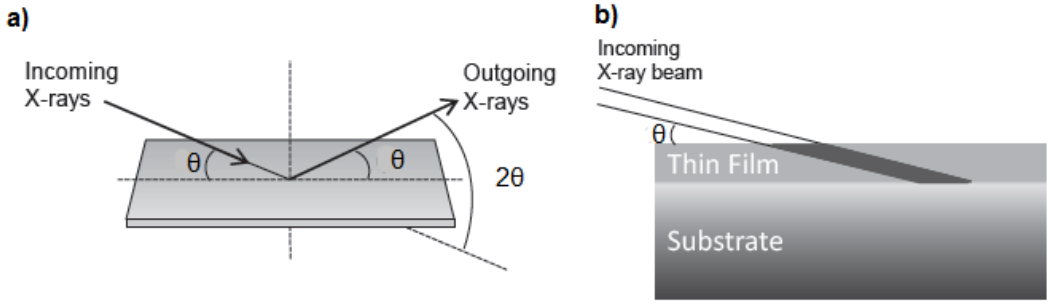

Figure 11: a) XRD geometries b) dependency of the probed film volume with the incoming angle θ [3]

The peak width is an often used parameter to evaluate the thin film morphology. A narrow peak in the XRD pattern indicates the present of a big grain or a single crystal and is defined by a low full width half maximum value. In contrast, a polycrystalline material exhibits broader peaks which result in a higher full width half maximum value.

6.3. Nanoindentation

Hardness is a measure of resistance to external mechanical actions such as scratching or indentation. Consequently, there are different techniques of the quantitative hardness, such as scratch, indentation, and rebound tests [35]. Besides empirical methods, a computational approach was recently suggested for prediction of hardness in terms of electronegativity [36].

In our experiments, nanoindentation is used, which implies that an indenter (diamond tip) is forced into the material surface under defined conditions of load [35]. Depending on the material and the applied load, the penetration depth is in a scale between nm and µm. Nanoindentation tests are common to determine the mechanical properties (e.g., hardness and indentation modulus) of thin films and can be considered as a nearly non-destructive technique [37,38].

Figure 12 shows a typical load-displacement curve, which is recorded during a loading/unloading circle, where h_{max} corresponds to the maximum penetration depth, h_r to the residual penetration depth, h_e to the elastic penetration depth, h_c to the depth of the contact circle, P_{max} to the maximal load, and dP/dh to the initial unloading stiffness [39]. Hardness (H) and indentation modulus, (E) are evaluated from the load-displacement curve according to Oliver and Pharr [40] and consequently calculated using the following formulas:

$$H = \frac{P_{max}}{A}, \tag{4}$$

$$\frac{1}{E_{eff}} = \frac{(1-\upsilon^2)}{E} + \frac{(1-\upsilon_i^2)}{E_i} \tag{5}$$

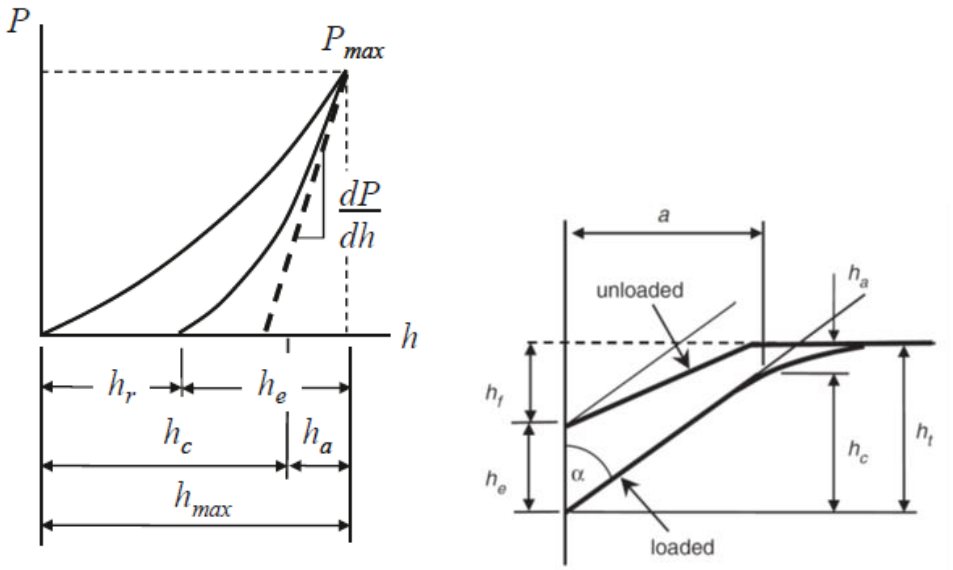

Figure 12: Load/displacement curve for an NbB_2 film [39,41]

The hardness of the deposited coatings was measured using a CSM Instruments Ultra Nano Hardness Tester (UNHT) equipped with diamond Berkovich tip. Load-displacement curves were acquired at 20 different spots on the film surface with an indentation depth set to 50 nm, a loading and unloading rate of 1.5 mN/min.

6.4. Contact resistance

A releasable junction between two conducting surfaces, which is intended to carry electrical current, can be explained as an electrical contact. As surfaces are not perfectly plane, just small portions of the apparent contact areas are in physical contact. Such a portion is called mechanical contact area ($A_{mechanical}$). The size and the distribution of these areas is defined by the contact force ($F_{contact}$) and the mechanical properties of the materials in contact ($H_{softest}$) [42].

$$A_{mechanical} = F_{contact}/H_{softest} \quad (6)$$

The areas which are in mechanical contact are however not in all cases conductive, since isolating surface oxides limit their conductivity. The area $A_{conductive}$, which is free of contaminants and surface oxides, is significantly smaller than the areas of mechanical contact [3]. Up to what extent the surface oxides are broken is depending on the mechanical properties of the contact materials, as well as on their chemical properties, which affect the hardness and thickness of the oxide. The

penetration of the surface oxide is also depending on the contact force, but there is no such simplification as for $A_{mechanical}$.

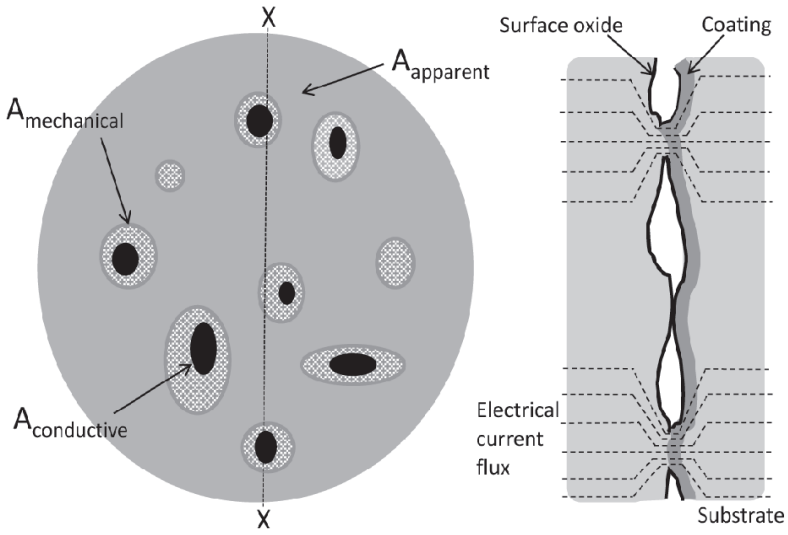

Figure 13: Schematics of a contact interface between a coated contact member and an uncoated contact member [2]

The relevant property of an electrical contact is the electrical contact resistance ($R_{contact}$). The electrical current flux over a contact junction is constricted to the $A_{conductive}$ spots. This effect leads to the so called constriction resistance, which can be calculated as followed

$$R_{constriction} = \frac{(\rho_1+\rho_2)}{4 \cdot A_{conductive}} \qquad (7)$$

where ρ_1 and ρ_2 are the resistivity of the contact members. For an electrical contact, $R_{constriction}$ depends on the distribution of the $A_{conductive}$ spots as well as on the total area of $A_{conductive}$ spots. For connectors which are coated, the film resistance (R_{film}) will also contribute to the contact resistance. As R_{film} and $R_{constrition}$ are independent from each other, the contact resistance can be expressed as followed

$$R_{contact} = R_{film} + R_{constriction} \qquad (8)$$

A custom-built set-up with an Au coated pin was used for measuring the electrical contact resistance. The contact resistance was calculated from the voltage drop over the contact junction while a constant current of 0.1 A was applied. The measurements were performed at three different spots on the film surface with a contact force of 1, 3 and 5 N.

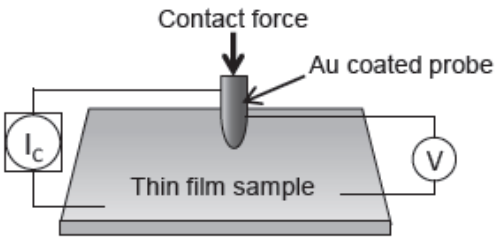

Figure 14: Draft of the contact resistance measurement set-up [3]

6.5. Elastic Recoil Detection Analysis

ERDA is an ion beam measurement technique which is used to determine elemental composition of surface near regions. This technique uses high-energy, high-mass projectiles bombarding the target material, causing an elastic recoil of its nuclei. The recoiling target atoms are measured to gain the information on target composition [43]. The strength of ERDA is the good mass resolution (> 0.1 at. %) and sensitivity for light elements such as B, N, O and C.

Iodine (36 MeV $^{127}I^{+8}$) is used as projectile atoms that penetrate into the film and eject the target atoms. The recoiled atoms are measured by a time of flight energy (ToF-E) detector. The time of flight of the recoiled atoms is detected by two carbon timing foils and a second detector measures the energy of the atoms. The atomic mass can be calculated by the following equation [44]:

$$E_i = \frac{M_i \cdot v^2}{2} => M_i = \frac{2 \cdot E \cdot \Delta t^2}{L^2} \quad (9)$$

where, Δt is the time of flight , L – traveled distance, and E – energy of the recoiled atoms.

6.6. Ball–on–disk

Friction is the resistance towards relative movement of two counter-parts in contact and is quantified by the friction coefficient μ, which is defined as the ratio between the tangential friction (F_F) force and the normal force (F_N).

$$\mu = {F_F}/{F_N} \quad (10)$$

One can distinguish between static and dynamic friction. Static friction is the force needed to start sliding, while dynamic friction is the force needed to maintain sliding. Dynamic friction, investigated in this work, can be divided into a ploughing (μ_p) and an adhesive component (μ_A) [45].

$$\mu = \mu_A + \mu_P \qquad (11)$$

The adhesive component is attributed to shear off material in the areas of real physical contact. The ploughing may take place, if one of the counterparts is much harder than the other [45].

Friction is a system parameter and not a specific material property. The acquired friction values depend on the roughness of the surfaces in contact, as well as on the ambient atmosphere (temperature and humidity) and lubrication [45].

The friction measurements were carried out using a ball–on–disk set-up in ambient air atmosphere with a relative humidity between 40 -50 % (Figure 15). As counter surface, stainless balls (100Cr6) with a radius of 6 mm were used. The track had a radius of 2.5 mm, the sliding speed was 0.1 m/s, and the contact force was 1N [3].

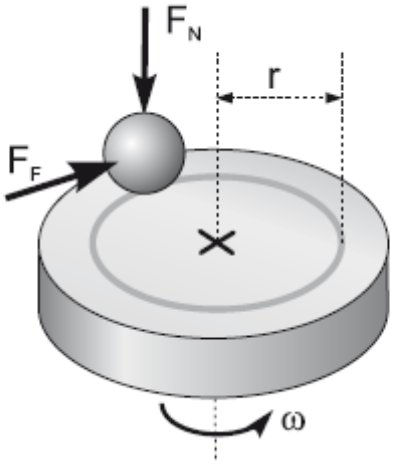

Figure 15: Scheme ball–on–disc setup [2]

6.7. Scanning electron microscopy

Scanning electron microscopy (SEM) is an important technique for imaging with high magnifications. The SEM uses a focused electron beam instead of visible light, and the Abbe limit shows that a higher spatial resolution can be achieved than with an optical microscopes [46]. An energy dispersive X-ray spectrometer allows analyzing the elemental composition.

A field emission cathode emits an electron beam which is accelerated by an electric field (between 5 and 20 kV) and focused on the sample surface by a setup of magnetic lenses. The sample and the electron gun are placed in a vacuum chamber to avoid interaction with the air. The primary electron beam interacts with the electronic structure of the sample atoms and the electrons are scattered

either elastically or inelastically (Figure 16). These interactions lead to the reflection of primary electrons (backscattered electrons, BSE), emission auger electrons (AE), secondary electrons (SE) and electromagnetic radiation used for EDS analysis. For all images within this thesis, the secondary electron collecting mode was used [47].

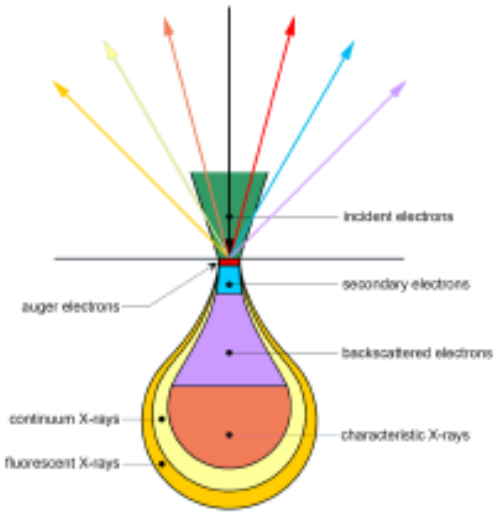

Figure 16: Pear shaped volume of electron interaction

7. Experimental setup

All thin films were synthesized using an UHV magnetron sputtering deposition system. Before all deposition processes, the chamber was evacuated to a base pressure below $3 \cdot 10^{-8}$ torr ($4 \cdot 10^{-8}$ mbar). The working gas pressure was constant at 3 mtorr ($4 \cdot 10^{-3}$ mbar). Up to four 2"-targets were mounted in a sputter down configuration and tilted towards the center of the substrate holder (Figure 17). The current on the magnetrons can be separately controlled in order to vary the film composition. The substrate holder is placed 14 centimeters below the targets and rotates during the deposition process, in order to guarantee the film homogeneity. The substrates are heated by a resistive heater placed below the substrate holder, and the substrate temperature is measured by a thermocouple, calibrated using an infrared pyrometer. The coatings were deposited at different temperatures ranging from RT to 700 °C. In order to simplify the SEM, XPS and hardness analysis, (001) silicon wafers with a thickness of 0.5 mm were used, while the 0.3 mm thick Si substrates were used for determination of internal stresses. Amorphous SiO_2 was used for the XRD and contact resistance measurements, while polished austenitic 316 L stainless steel substrates were used for tribological measurements.

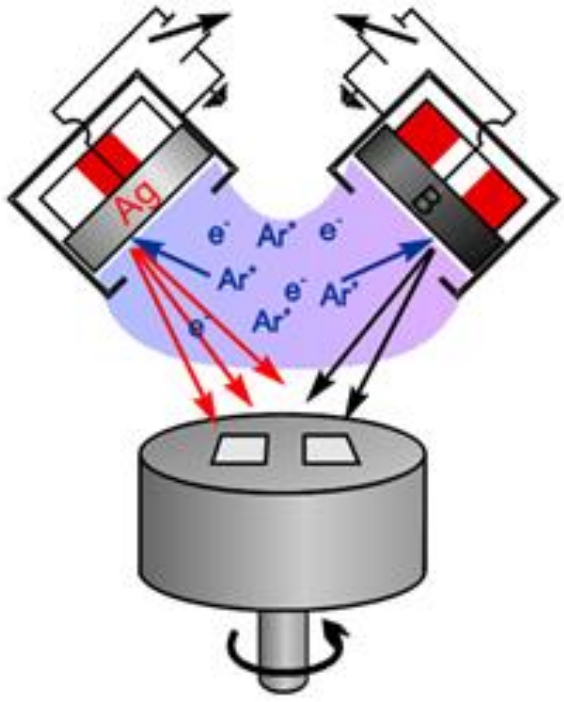

Figure 17: Sketch of co-sputter deposited from the silver and boron targets [2]

However, it is worth mentioning that the supplied niobium diboride target (99.5% purity) contained crystalline NbC next to NbB_2.

Prior to all depositions the substrates were pre-heated to the desired temperature for at least 90 minutes to minimize the temperature gradient. The substrates were cleaned by plasma etching for 10 minutes and a pre-sputter process was carried out for 15 minutes. A thin Ti adhesion layer was deposited prior to the boron-alloyed silver and Nb–Ag–B coatings. A substrate bias of -50 V was applied for all films within this work.

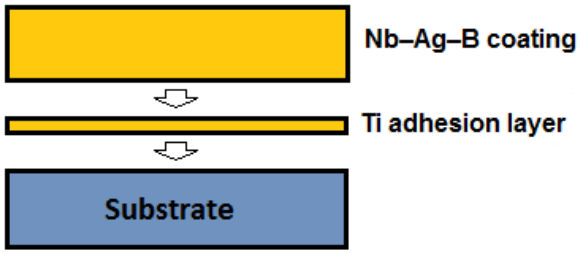

Figure 18: Layer sequence for Nb–Ag–B coatings [48]

8. Results and discussion

Within the framework of this thesis, two coating systems, Ag–B and Nb–Ag–B, were investigated. The crystalline AgB_2 is of great interest from the viewpoint of fundamental research. The boron-alloyed silver and Nb–Ag–B thin films were investigated for possible industrial applications.

8.1. AgB_2

The aim of this study was to investigate the possibility of depositing a crystalline AgB_2 phase in the UU sputter equipment. In the first series of experiments, Ag–B calibration films were co-sputter deposited from the silver and boron targets to determine the current settings leading to the 1:2 stoichiometry, i.e, AgB_2. The current on the boron target was kept constant at 100 mA, while the current on the silver target was changed as follows: 5, 11, 12 and 50 mA. The substrates were not exposed to an external heating, i.e., the substrate heating occurred only by the kinetic energy transfer from the arriving sputtered particles. Figure 19a shows the GIXRD patterns from the calibration films. The film deposited with I_{Ag}= 5 mA (20 at.% Ag) is nearly XRD amorphous. There are only small broad peaks indicating nanocrystalline silver particles surrounded by an amorphous boron matrix. The films deposited with I_{Ag}= 11, 12, and 50 mA (29, 40, and 80 at.% Ag, respectively), exhibit more pronounced silver reflexes, which are still broad indicating the presence of nanocrystalline silver particles. With increasing the target current and thus the Ag-content, the FWHM of the (111) peak decreases from 2.6 (20 at.% Ag) to 0.8 (80 at.% Ag) indicating the grain growth, cf. Figure 19b. The coating with 29 at.% Ag exhibits the closest Ag-content to the 1:2 stoichiometric AgB_2 with ~33 at.% Ag. Thus, for further experiments, the current on the silver target was kept constant at I_{Ag}= 11 mA.

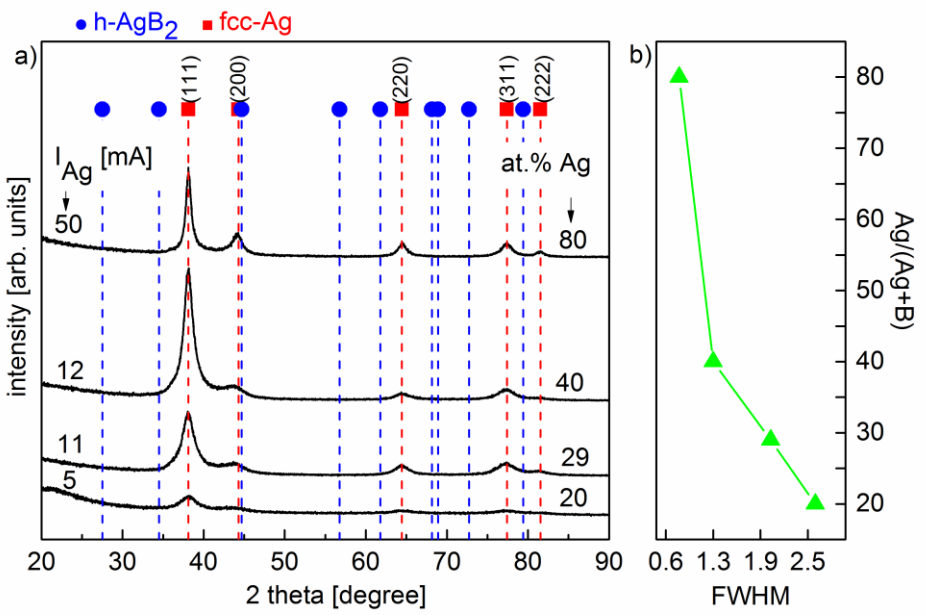

Figure 19: a) GIXRD patterns and b) FWHM of the (111) Ag peak, for the films containing 20, 29, 40, and 80 at.% Ag

The crystalline AgB_2 is suggested to be metastable [49] and the ideal deposition temperature has not been determined yet. However, Folkenant et al. [4] has recently observed, that the silver-containing films are much denser and homogenous when deposited without external heating as compared to higher deposition temperatures, at which Ag diffuses to the film surface. In order to optimize the substrate temperature, T_{sub}, external heating was applied (resistive heater placed below the substrate holder) in the temperature range from RT to 500 °C. Figure 20a shows the GIXRD patterns of the Ag–B coatings deposited with I_{Ag}= 11 mA at three different temperatures: RT, 300 °C, and 500 °C (RT implies that no external heating was applied, i.e., the substrates were only heated by the arriving high-energetic sputtered particles). Throughout all experiments, no indication of a possible AgB_2 phase was observed. An increase of the substrate temperature results only in sharpening of the Ag-reflexes, reducing the FWHM of the (111) peak from 2.01 at T_{sub}= RT to 0.38 and 0.37 for T_{sub}= 300 °C, and 500 °C respectively, cf. Figure 20b. This indicates the coarsening of the Ag-grains with the increasing temperature.

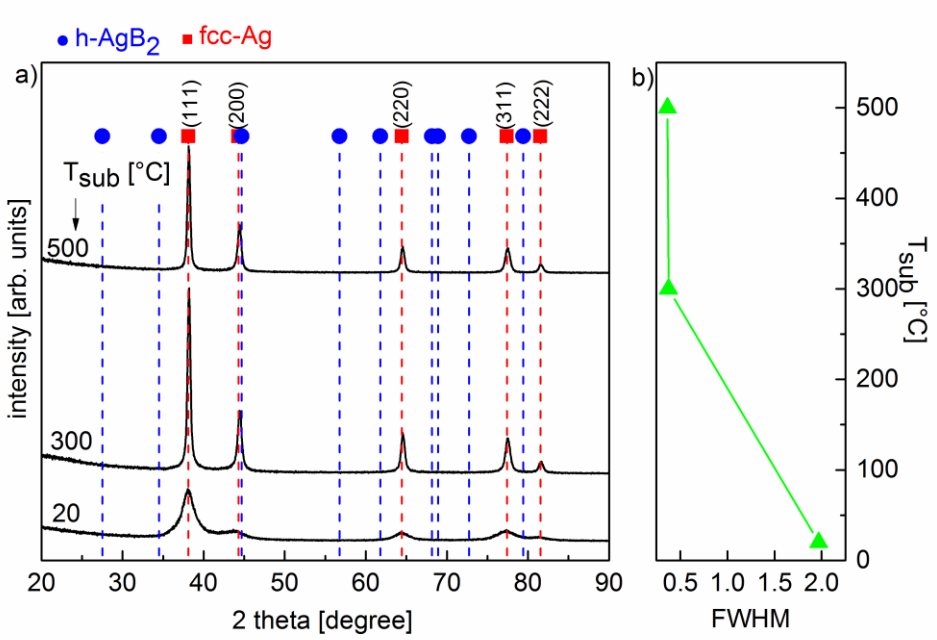

Figure 20: a) GIXRD patterns and b) FWHM of the (111) Ag peak, for the films containing 29 at.% Ag with T_{sub}= RT, 300 ,and 500 °C

Within our experiments we determined the current settings leading to the 1:2 stoichiometry, i.e, AgB_2. For this setting, we investigated the influence of T_{sub} on the film microstructure. However, based on our results we cannot provide additional information to prove the existence of a crystalline AgB_2 phase.

8.2. Boron–alloyed silver

Silver is a widely used material for electrical contacts, since it exhibits excellent electrical properties [50] and can easily be deposited as a thin film [51]. However, for new sliding electrical applications silver is not suited due to the high COF and the high wear rate [51]. One approach to reduce the friction coefficient of Ag is the addition of boron, which should form the lubricant H_3BO_3 [52] during operation.

One film containing 80 at.% Ag and one Ag reference sample were deposited at RT (RT implies that no external heating was applied, i.e., the substrates were only heated by the arriving high-energetic sputtered particles). The GIXRD patterns (Figure 21) of the boron–alloyed Ag and the Ag reference coatings show only pronounced fcc-Ag reflexes. With increasing Ag-content, the

XRD peaks increase in intensities, and FWHM of the (111) peak decreases from 0.81 (80 at.% Ag) to 0.32 (100 at.% Ag) (as estimated from the GIXRD patterns, Figure 21).

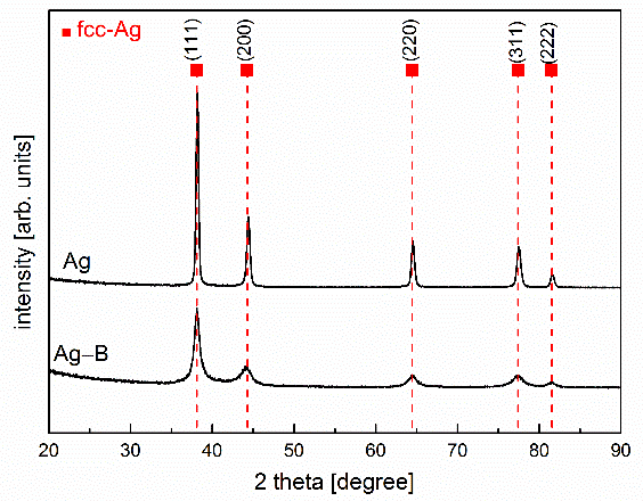

Figure 21: GIXRD patterns of the boron–alloyed and Ag reference samples deposited at RT

For both coatings a standard friction test against a stainless steel balls was carried out. On the Ag reference sample the COF was ~0.59, which correlates well with literature (Ag vs steel 0.55 [45]). For the boron-alloyed coating the COF was observed to be ~0.33. The wear track of the Ag reference sample is significantly wider than the one of boron-alloyed Ag film. In the wear track of Ag reference sample big areas of film delamination were observed (Figure 22 a). In contrast only partial film delamination was observed in the wear track of the boron-alloyed Ag film (Figure 22 b). The significantly lower COF for the boron-alloyed coating compared to the pure Ag coating can be explained by the formation of the friction product B_2O_3 in the wear track (as derived from the XPS measurement), which prevents silver from delaminating.

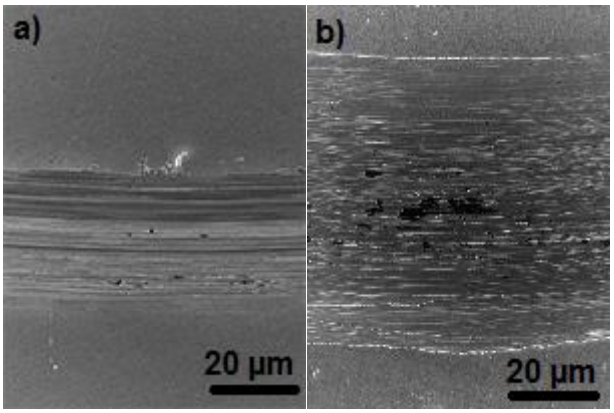

Figure 22: SEM images of the wear tracks after ball–on– disk test against stainless steel for a) boron-alloyed Ag and b) Ag reference sample

For sliding electrical contacts, both counterparts are noble metals (or alloyed noble metals) and therefore, the COF was also measured against an Ag pin. The COF of the boron-alloyed Ag coating against an Ag pin was observed to be ~1.07 (Figure 23).

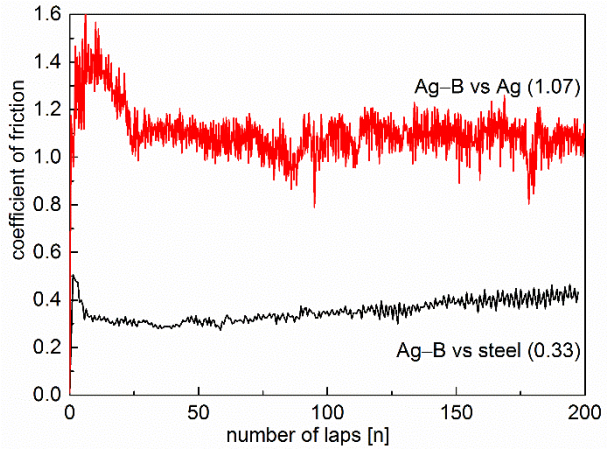

Figure 23: Measured friction curves of a boron–alloyed Ag against a stainless steel balls and against an Ag pin and measured friction curves of pure Ag against a stainless steel

For both coatings the contact resistance was measured with the contact force ranging from 1 to 5 N. The contact resistance for the Ag reference sample was observed to remain nearly constant at 5.5 ± 0.5 mΩ for all contact loads. For the boron-alloyed Ag the contact resistance decreased from 20.3 ± 0.2 mΩ (at 1 N) to 16.2 ± 0.1 mΩ (at 5 N). The drop of contact resistance has to be reviewed critically for this sample, since cracks formed due to the contact load of 5 N. The added poorly

conducting boron acts as scattering centers for electrons and leads to an increase of film resistance, which in turn contribute to a higher contact resistance.

Based on our results we can conclude that alloying silver with boron leads to significant reduction of COF against stainless steel. In future industrial applications both counterparts will be noble metals and therefore, boron-alloyed silver is not suitable due to the high COF against noble metal counterparts.

8.3. Development of new Nb–Ag–B thin films

In the first step, we aimed at reproducing the promising NbB_2 coatings obtained by Nedfors [1]. Furthermore, in order to enhance the electrical properties, NbB_2 was alloyed with different amounts of silver. For this purpose, the current on the NbB_2-target was kept constant at 150 mA, while the current on the Ag-target was varied from 0 to 25 mA.

Using the same deposition chamber and similar deposition conditions as Nedfors [1], we obtained a strongly (001) textured NbB_2 film (as revealed by the θ-2θ scan, Figure 24) with the cell parameters a = 3.08 Å and c = 3.29 Å (as estimated from the GIXRD pattern, Figure 24). Nedfors, in contrast, obtained polycrystalline, weakly (001) preferentially oriented NbB_2 films with the cell parameters a = 3.12 Å and c = 3.28 Å [1]. The difference in the coatings microstructure can apparently be explained by a higher base pressure used in the current work [1]. This, in turn, results in a higher oxygen concentration in the sputtering atmosphere as well as in the synthesized coating.

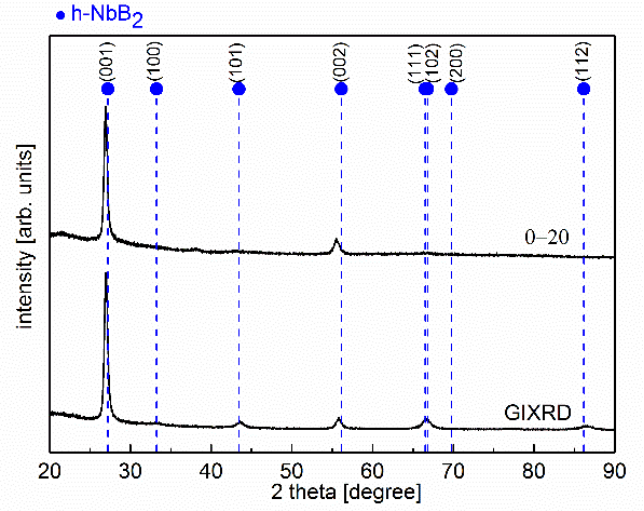

Figure 24: θ-2θ and GIXRD patterns of the NbB_2 film deposited at 300 °C

The GIXRD patterns of Nb–Ag–B films with different Ag-content are presented in Figure 25. The addition of 16 and 23 at.% Ag results in the growth of nanocrystalline silver particles and crystalline NbB_2, and a reduced grain size for NbB_2 is indicated by increasing FWHM of the (001) NbB_2 peak. An increase of Ag content to 54 at.% leads to the growth of nanocrystalline Ag, surrounded by XRD amorphous NbB_2.

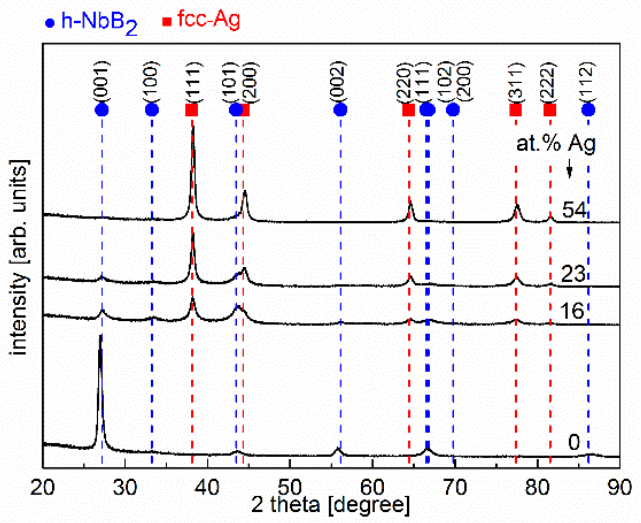

Figure 25: GIXRD patterns of Nb–Ag–B films with varying Ag-content deposited at 300 °C

The microstructure (fracture cross-section, Figure 26 a-d) and the surface (top-view, Figure 26 e-h) of the film have been analyzed using SEM. The SEM cross-section of the NbB_2 film (Figure 26 a) exhibits a dense columnar microstructure. The film thickness is around 510 nm, which corresponds to a deposition rate of ~2.2 nm/min. For the film containing 16 at.% Ag (Figure 26 b) a change from a dense to a porous microstructure was observed. The films with 23 at.% (Figure 26 c) and 54 at.% (Figure 26 d) Ag-content exhibit the for silver typical porous microstructure. The SEM top-view of the NbB_2 shows a smooth surface with some defects on it. For the film with 16 at.% Ag-content bright silver particles are visible on the surface. The films containing 23 at.% and 54 at. % Ag exhibit rough surfaces.

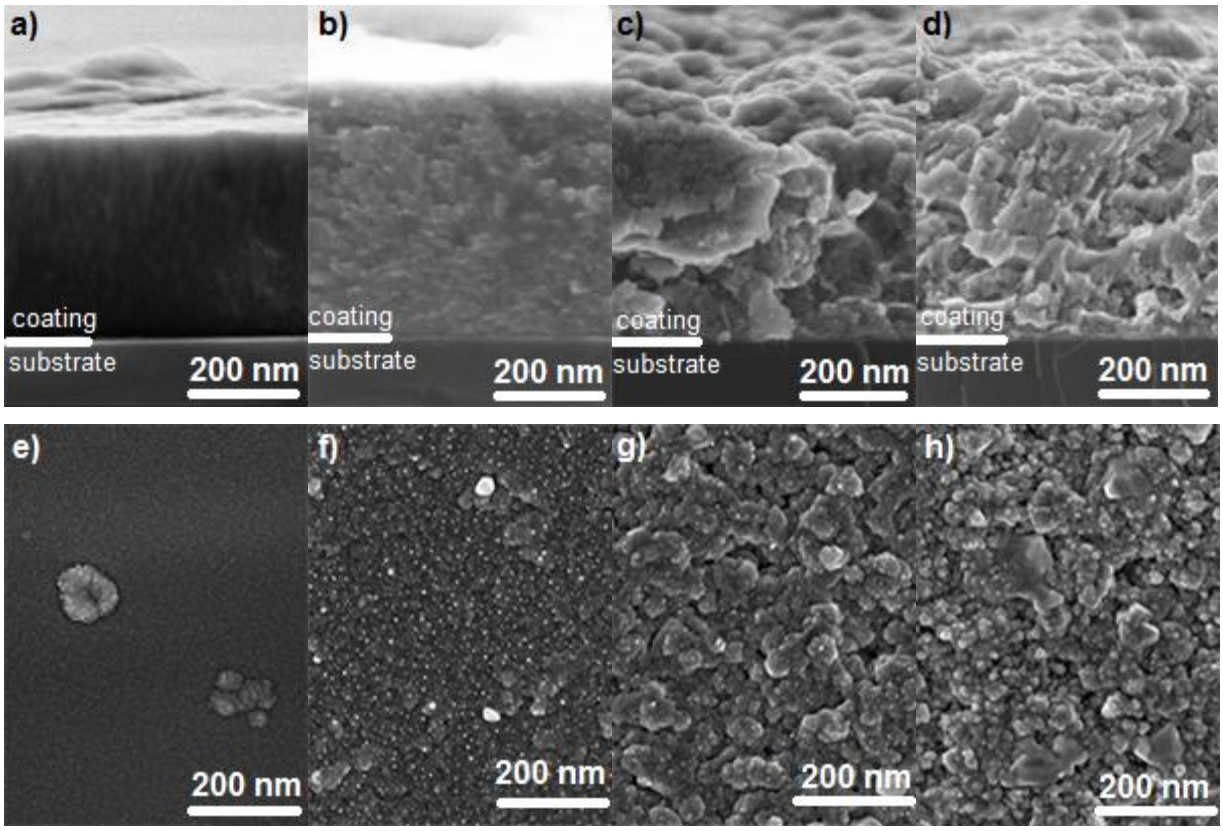

Figure 26: SEM fracture cross-sections of Nb–Ag–B films with varying Ag-content (at.%) a) 0 b) 16 c) 23 d) 54 and SEM top-view of Nb–Ag–B films with varying Ag-content (at.%) e) 0 f) 16 g) 23 h) 54

Diborides of the IV-group metals show typically a rather high friction coefficient against stainless steel as it was reported for TiB_2 with μ ~0.75 (ambient air, 1 N contact force) [53]. Surprisingly, the superhard NbB_2 (42 GPa) was found to exhibit COF of 0.16 (ambient air, 1 N contact force) [1] and for VB_2 an ever lower COF of 0.05 (annealed air, 5 N contact force) [52]. Such low friction coefficients were explained by the formation of a H_3BO_3 layer in the wear track in agreement with the two-step reaction:

$$2B + {}^3/_2\, O_2 \rightarrow B_2O_3 \qquad (12)$$

$${}^1/_2\, B_2O_3 + 3({}^1/_2\, H_2O) \rightarrow H_3OB_3 \qquad (13)$$

Here, we also investigated the influence of the Ag-addition on the friction coefficient of NbB_2. Addition of Ag reduces COF of NbB_2 from ~0.91 (0 at.% Ag) to ~0.35 (54 at.% Ag), cf. Figure

28. For the coatings containing 0 and 54 at.% Ag, stable friction curves were observed after a running-in effect of around 400 laps. Film delamination was observed in all Ag-containing films (Figure 27 c,d). The formation of wear debris, as well as film delamination, leads to the unsteady friction curves of the coatings containing 16 and 23 at.% Ag. For 0 at.% Ag, i.e. NbB_2, the COF was found to be 0.91, which correlates well with the published values for diborides (i.e. CrB_2 [54]), but significantly overcomes the COF of Nedfors superhard NbB_2. In contrast to the low-frictional NbB_2 coatings obtained by Nedfors, partial film delamination and crack formation were observed in our wear track (Figure 27 a,b). The formation of the lubricant H_3BO_3 would be expected for our NbB_2 coating, but during operation only the friction product B_2O_3 was formed.

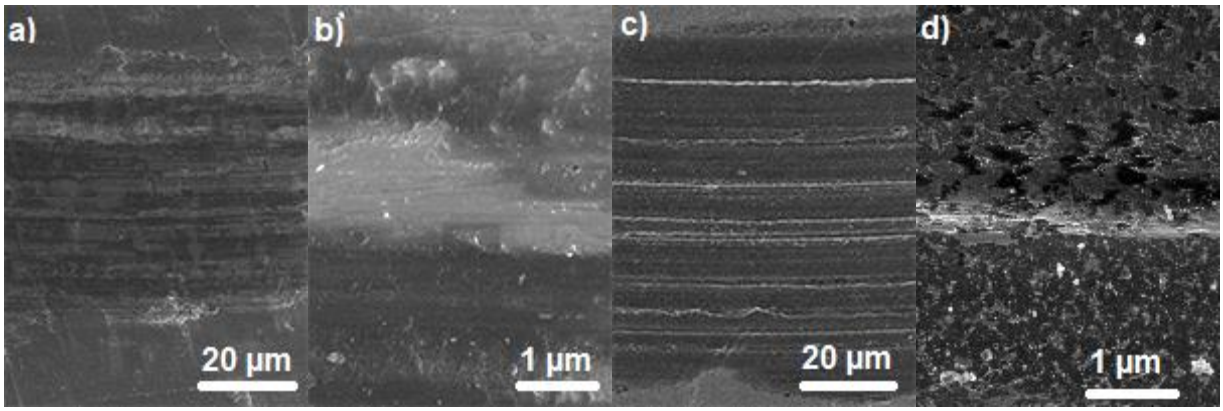

Figure 27: SEM images, taken at two different magnifications, of the wear tracks after ball–on–disk test against stainless steel for (a), (b) the NbB_2 film, and (c), (d) the Nb–Ag–B film containg 23 at. % Ag

Apparently the film texture has a negligible influence on the friction coefficient, since similar COFs µ ~0.9 were observed for weakly (001) (produced by Uppsala University thin-film group, unpublished data) and for strongly (001) textured NbB_2 films. The friction values obtained for 23 and 54 at.% Ag are lower than the friction values for pure Ag against steel (0.55) [45] which can be attributed to the formation of B_2O_3 in the wear track. All results were confirmed by a second identical test performed on a different spot for each film.

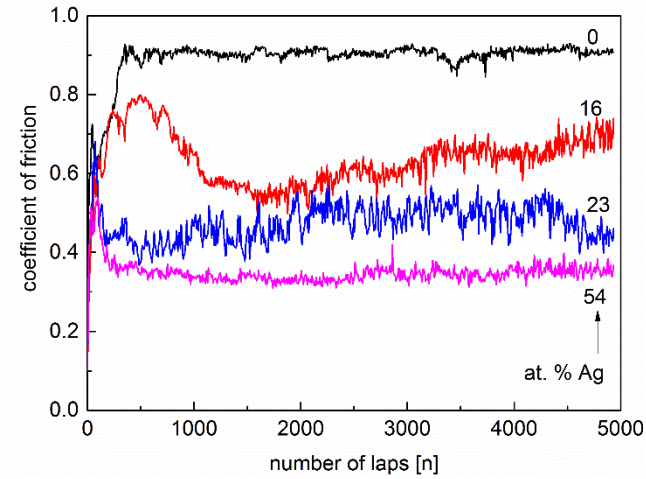

Figure 28: Measured friction curves for Nb–Ag–B films when sliding against a stainless steel ball at a relative humidity of 50 %

Figure 29 shows the mechanical properties of Nb–Ag–B films, obtained by nanoindentation, plotted as a function of Ag-content. The NbB_2 film exhibits a hardness of 31 ± 2 GPa and thus is ~10 GPa harder than bulk NbB_2 (21 GPa [55]), but still significantly softer than the superhard NbB_2 (42 GPa [1]). Nedfors' assumption that a fine-tuning of the process towards stronger (001) orientated NbB_2 leads to an increase of hardness could not be confirmed within our work. The indentation modulus of 313 ± 10 GPa for the NbB_2 film is nearly twice as low as the 580 GPa published in Ref. [1]. The addition of 16 at.% Ag leads to a drop in hardness from 31 ± 2 GPa to 16.2 ± 3.2 GPa, which continues to decrease to 2.3 ± 0.4 GPa for the film containing 54 at% Ag. The indentation modulus dropped from 313 GPa (0 at.% Ag) to 46 GPa (54 at.% Ag), and correlates well with the trend observed for the hardness.

As mentioned in paragraph 6.3, we have to consider the film microstructure when measuring the hardness with nanoindentation technique. For the films with high Ag-content, we face the problem of high porosity and surface roughness. During hardness measurements, the tip penetrates into the films (23 and 54 at% Ag) by more than 10 percent of the film thickness (> 95 nm), and therefore, the hardness values can be influenced significantly by the substrate. Another problem is that for films with an increased Ag-content less loading/unloading circles were taken into account, which can lead to errors in the statistical analysis.

The residual stresses were estimated by applying Stoney's equation on curvature measurements of deposited Nb–Ag–B films on a Si(001) wafers [56]. The compressive residual stresses within our Nb–Ag–B films decrease from 2.3 to 0.13 GPa and thus correlates excellently with the hardness.

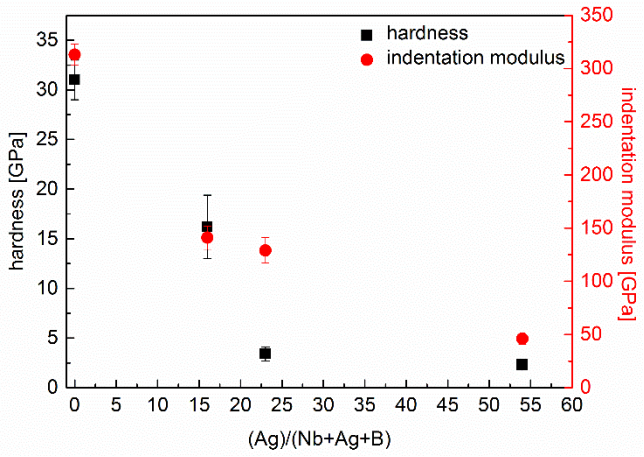

Figure 29: Mechanical properties of the different Nb–Ag–B films obtained using nanoindentation

Contact resistance measurements were carried out on selected samples. For NbB_2 the contact resistance remained constant at 1.2 ± 0.3 Ω within the contact force range from 1 to 5 N. Such a low contact resistance for NbB_2 was achieved by Nedfors [1] only for the contact forces of 5 N and higher. For the softer films, a larger electrical contact area is accessible under the same contact load resulting in a lower contact resistance. Silver is one of the best conducting metals [50], and the addition of 16 at.% Ag (which decreases the hardness as well) leads to an expected reduction of contact resistance to 0.5 ± 0.1 Ω within the contact force range.

XPS analysis was performed for the NbB_2 film in order to gain information on the chemical bonds. In the B1s spectrum, several peaks can be clearly distinguished (Figure 30). The B1s spectrum of the NbB_2 single crystal has recently been studied in detail by Aizawa et al. [57] and the peaks are listed in Table 1. The main peak (188.7 eV) originates from B, bonded to Nb in the bulk of the crystal (B–Nb_b). They also observed a peak at 1.6 eV lower binding energy (187.1 eV), which is attributed to the B bonds in the surface layer (B–Nb_s). This peak was explained by a core-level shift generated by a coordination change in the surface layer compared to the bulk boron atoms and was confirmed by DFT calculations [57]. Furthermore, Aizawa found a peak in between, at 187.8 eV, which was attributed to defects (B–Nb_d) in the crystal. Although this peak was not investigated precisely, it is most likely that the peak originates from the boron atoms close to the boron

vacancies in the structure [57]. Matiensen et al. found the binding energy of amorphous boron (B–B) to be 187.5 eV [58].

Table 1: A summary of the fitted peaks and their energies in the XPS B1s spectrum

Chemical bond	Binding energy (eV)		
	reference single crystal	Nedfors [1]	this work
B-Nb_b	188.7 [57]	188.8	188.6
B-Nb_d	187.8 [57]	188.0	187.9
B-Nb_s	187.1 [57]	187.2	187.1
B-B	187.5 [58]	187.5	187.5

Based on the data we can split our B1s of the spectrum of the films into four respectively three peaks. The pure NbB_2 exhibit a main feature at 188.6 eV, which has 0.1 eV lower binding energy than the main feature of single crystal NbB_2. The difference of 0.1 eV is below the instrumental error. The B-Nb_d and the B-Nb_s were observed at 0.7 eV and 1.5 eV lower binding energies than the main feature, respectively. The B-Nb_d peak at 187.9 eV has a rather high intensity compared to the literature, which leads to the assumption of a higher concentration of boron vacancies in the film, and therefore, the film is assumed to be substiochiometric. The fourth peak can indicate the presence of boron on the interface between the diboride grains. The addition of Ag leads to reduced B-Nb_s interactions and therefore, the B1s spectrum of the films containing Ag can be fitted with only three peaks. Furthermore, an increasing Ag-content in the films leads to increasing B-Nb_d and decreasing B-Nb_b contributions to the B1s spectrum. For the film containing 54 at. % Ag the B-Nb_d intensity exceeds B-Nb_b intensity resulting in a peak shift towards lower binding energies.

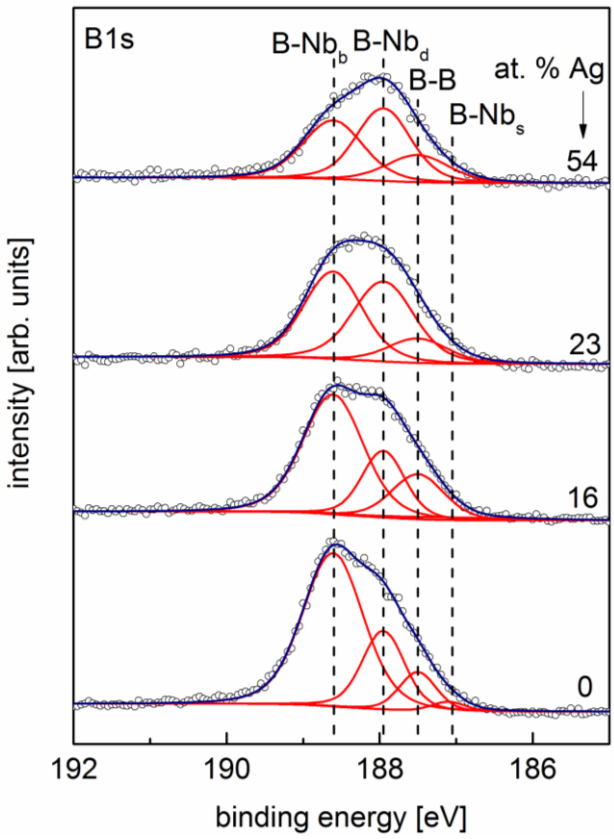

Figure 30: XPS B1s spectrum of an Nb–Ag–B film acquired after 30 min of sputtering with 200 eV Ar+-ions. B–Nbb, B–Nbd, and B–Nbs correspond to B atoms in the bulk, near a defect, and at the surface. B–B corresponds to amorphous boron

In order to investigate which friction products were formed in the wear track, the XPS spectrum was acquired (Figure 31) after the ball-on-disk measurements. The peak at 192.45 eV corresponds exactly to the position of B_2O_3 [59]. From this peak we can conclude, that H_3BO_3 was not present in the wear track after the tribological tests, since the formation of H_3BO_3 would lead to a peak shift towards higher binding energies. The present of B_2O_3 in the wear track was confirmed by Raman spectroscopy (not shown).

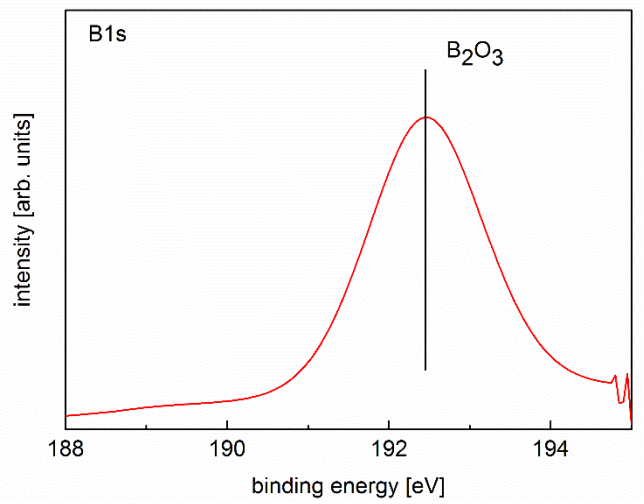

Figure 31: Fitted XPS B1s of the wear track on our NbB_2 film after ball–on–disk measurement

9. Conclusions

The aim of this thesis was to develop new Ag–B and Nb–Ag–B-based thin film materials for electrical contact applications. This work can be divided into three thematic subchapters. All films have been synthesized by physical vapor deposition and their mechanical and electrical properties have been investigated.

In the first part, we investigated the structural properties of our Ag–B films with a focus on the possible formation of a crystalline AgB_2 phase. Films with various Ag/B-ratios were deposited using different substrate temperatures by co-sputtering of pure Ag and B targets. However, within our experiments, no indication of a crystalline AgB_2 phase was observed.

In the second part, we focused on the tribological properties of Ag–B films with a boron content of 20 at.%. It was expected that the addition of boron would lead to the formation of the lubricant boric acid (H_3BO_3) in the wear track. Though our experiments showed the formation of only B_2O_3 (no indication of H_3BO_3). The B_2O_3 layer in the wear track contributes to the significant improvement of COF from boron-alloyed Ag coatings (0.33) compared to pure Ag-coatings (0.55). However, the boron-alloyed silver is not suitable for future industrial applications due to the high COF against noble metal counterparts.

In the third part, the mechanical and electrical properties of Nb–Ag–B films were investigated. The films were co-sputtered from the compound NbB_2 and pure Ag targets, and the silver content in the films was varied from 0 up to 54 at.%. The NbB_2 (0 at.% Ag) film is strongly (001) textured and exhibits a hardness of 31 ± 2 GPa. A reasonable high friction coefficient (0.91) was measured against stainless steel, and the XPS analysis showed that only B_2O_3 (without lubricant H_3BO_3) was formed as friction product in the wear track. An increase of Ag content up to 0.54 at.% results in continuous deterioration of hardness from 31 ± 2 to 2.3 ± 0.4 GPa, but also in significant reduction of the friction coefficient from 0.91 to 0.35. The contact resistance was observed to be 1.2 ± 0.3 Ω for NbB_2 and 0.5 ± 0.1 Ω for the film containing 16 at.% Ag. Based on our results we can conclude, that Nb–Ag–B films on Ag content up to 54 at.% are not suitable for sliding electrical contacts.

List of Figures

List of Abbreviations and Symbols

BSE ..... back scattered electron

CVD ..... chemical vapor deposition

COF ..... coefficient of friction

DC ..... direct currency

E_b ..... binding energy

E_k ..... energy of the photoelectrons

ERDA ..... elastic recoil detection analysis

ESCA ..... electron spectroscopy for chemical analysis

FWHM ..... Full Width Half Maximum

F_F ..... friction force

F_N ..... normal force

GIXRD ..... grazing incidence x-ray diffraction

h_{max} ..... maximum penetration depth

h_c ..... depth of the contact circle

MeB_2 ..... metal diborides

P_{max} ..... maximal load

PVD ..... physical vapor deposition

SEM ..... scanning electron microscopy

SZM ..... structure zone model

T_c ..... transition temperature

T_h ..... homologous temperature

T_{sub} ..... substrate temperature

ToF-E ..... time of flight energy

UHV ..... ultra high vacuum

XPS..... X-ray photoelectron spectroscopy

XRD ..... X-ray diffraction

Δt ..... time difference

λ ..... wave length

Φ ..... work function

Ω ..... electrical resistivity

Bibliography

[1] N. Nedfors, O. Tengstrand, J. Lu, P. Eklund, P.O.Å. Persson, L. Hultman, U. Jansson, Surface & Coatings Technology 257 (2014) 295–300.

[2] E. Lewin, Design of Carbide-Based Nanocomposite Coatings, Acta Universitatis Upsaliensis, (2009).

[3] N. Nedfors, Synthesis and Characterization of Multifunctional Carbide- and Boride-Based Thin Films, Acta Universitatis Upsaliensis, (2014).

[4] M. Folkenant, Synthesis and Characterization of Amorphous Carbide-Based Thin Films, Acta Universitatis Upsaliensis, (2015).

[5] W. Obrowski, Die Naturwissenschaften 48 (1961) 428–428.

[6] H. Euchner, P.H. Mayrhofer, Thin Solid Films 583 (2015) 46–49.

[7] T. Massalski, Binary Alloy Phase Diagrams, American Society for Metals, Metals Park Ohio, (1986).

[8] P. Vajeeston, P. Ravindran, C. Ravi, R. Asokamani1, Physical Review B 63 (2001) 1–12.

[9] A.N. Kolmogorov, S. Curtarolo, Physical Review B - Condensed Matter and Materials Physics 74 (2006) 14.

[10] C. Ying, E. Zhao, L. Lin, Q. Hou, Modern Physics Letters B 28 (2014) 1450213.

[11] J. Nagamatsu, N. Nakagawa, T. Muranaka, Y. Zenitani, J. Akimitsu, Nature 410 (2001) 63–64.

[12] C.A. Nunes, D. Kaczorowski, P. Rogl, M.R. Baldissera, P.A. Suzuki, G.C. Coelho, A. Grytsiv, G. André, F. Boureé, S. Okada, Acta Materialia 53 (2005) 3679–3687.

[13] I.R. Shein, N.I. Medvedeva, a. L. Ivanovskii, Physics of the Solid State 43 (2001) 2213–2218.

[14] S.K. Kwon, S.J. Youn, K.S. Kim, B.I. Min, 2 (2001).

[15] R. Tomita, H. Koga, T. Uchiyama, I. Iguchi, Journal of the Physical Society of Japan 73 (2004) 2639–2641.

[16] A. K.M. A Islam, F. Parvin, F.N. Islam, M.N. Islam, A. T.M.N. Islam, I. Tanaka, Physica C: Superconductivity and Its Applications 466 (2007) 76–81.

[17] F. Wald, R.W. Stormont, Journal of the Less Common Metals 9 (1965) 423–433.

[18] J. Pelleg, M. Rotman, M. Sinder, Physica C: Superconductivity 466 (2007) 61–64.

[19] M. Ohring, Materials Science of Thin Films, (2001).

[20] William D Westwood, Sputter Deposition, Education Committee, AVS, (2003).

[21] K. Wasa, M. Kitabatake, H. Adachi, Thin Film Materials Technology: Sputtering of Compound Materials, William Andrew, (2004).

[22] G.H. Gilmer, M.H. Grabow, JOM 39 (2012) 19–23.

[23] I. Petrov, P.B. Barna, L. Hultman, J.E. Greene, Journal of Vacuum Science & Technology

A: Vacuum, Surfaces, and Films 21 (2003) S117.

[24] P.H. Mayrhofer, Oberflächentechnik, (2014).

[25] B. Movchan and A. Demchishin, Phys. Met. Metallogr. 28 (1969) p. 653.

[26] J.A. Thornton, Journal of Vacuum Science and Technology 11 (1974) 666.

[27] R. Messier, Journal of Vacuum Science & Technology A: Vacuum, Surfaces, and Films 2 (1984) 500.

[28] A. Anders, Thin Solid Films 518 (2010) 4087–4090.

[29] S. Hüfner, Photoelectron Spectroscopy, Springer Berlin Heidelberg, Berlin, Heidelberg, (1996).

[30] L. Spieß, G. Teichert, R. Schwarzer, H. Behnken, C. Genzel, Moderne Röntgenbeugung, Vieweg+Teubner, Wiesbaden, (2009).

[31] http://www.microscopy.ethz.ch/bragg.htm (accessed May 20, 2015)

[32] B. Kramer, ed., Advances in Solid State Physics, Springer Berlin Heidelberg, Berlin, Heidelberg, (2001).

[33] P.F. Fewster, Reports on Progress in Physics 59 (1999) 1339–1407.

[34] S.-L. Chang, Journal of Physics and Chemistry of Solids 62 (2001) 1765–1775.

[35] W. Callister, D. Rethwisch, Materials Science and Engineering: An Introduction, (2007).

[36] K. Li, P. Yang, D. Xue, Acta Materialia 60 (2012) 35–42.

[37] S.H. Chen, L. Liu, T.C. Wang, International Journal of Solids and Structures 44 (2007) 4492–4504.

[38] R. Saha, W.D. Nix, Acta Materialia 50 (2002) 23–38.

[39] A.C. Fischer-Cripps, (2011) 21–38.

[40] W.C. Oliver, G.M. Pharr, Journal of Materials Research 7 (1992) 1564–1580.

[41] A.C. Fischer-Cripps, Surface and Coatings Technology 200 (2006) 4153–4165.

[42] R. Holm, Electric Contacts : Theory and Applications, Springer, (2000).

[43] A. Khatibi, J. Palisaitis, C. Höglund, A. Eriksson, P.O.Å. Persson, J. Jensen, J. Birch, P. Eklund, L. Hultman, Elsevier, (2011).

[44] B. Schmidt, K. Wetzig, Ion Beams in Materials Processing and Analysis, Springer Science & Business Media, (2012).

[45] K. Holmberg, A. Matthews, Coatings Tribology: Properties, Mechanisms, Techniques and Applications in Surface Engineering, Elsevier, (2009).

[46] C. Cremer, Physik in Unserer Zeit 42 (2011) 21–29.

[47] J. Goldstein, Scanning Electron Microscopy and X-Ray Microanalysis, Third Edit, Springer, (2003).

[48] C. Sabitzer, C. Steinkellner, C.M. Koller, P. Polcik, R. Rachbauer, P.H. Mayrhofer, Surface and Coatings Technology (2015).

[49] I.R. Shein, N.I. Medvedeva, A.L. Ivanovskii, (2004).

[50] G. Fasching, Werkstoffe Für Die Elektrotechnik, (2005).

[51] J. Sundberg, F. Mao, A.M. Andersson, U. Wiklund, U. Jansson, Journal of Materials Science (2012) 1–9.

[52] A. Erdemir, Tribology Letters 8 (2000) 97–102.

[53] J.T. Ok, I.W. Park, J.J. Moore, M.C. Kang, K.H. Kim, Surface and Coatings Technology 200 (2005) 1418–1423.

[54] N. Nedfors, D. Primetzhofer, L. Wang, J. Lu, L. Hultman, U. Jansson, Surface and Coatings Technology 266 (2015) 167–176.

[55] T. Lundström, B. Lönnberg, I. Westman, Journal of the Less Common Metals 96 (1984) 229–235.

[56] G.C.A.M. Janssen, M.M. Abdalla, F. van Keulen, B.R. Pujada, B. van Venrooy, Thin Solid Films 517 (2009) 1858–1867.

[57] T. Aizawa, S. Suehara, S. Hishita, S. Otani, M. Arai, Physical Review B 71 (2005) 165405.

[58] D.N. Hendrickson, J.M. Hollander, W.L. Jolly, Inorganic Chemistry 9 (1970) 612–615.

[59] J.F. Moulder, Handbook of X-Ray Photoelectron Spectroscopy: A Reference Book of Standard Spectra for Identification and Interpretation of XPS Data, (1992).